CDD *press*

Check for updates

ARTICLE

eIF4A3 regulates the TFEB-mediated transcriptional response via GSK3B to control autophagy

Despoina Sakellariou [ID][1], Matteo Tiberti[1], Thomas H. Kleiber[1], Lorea Blazquez[2,3,4], Aida Rodríguez López[1], Marie Holm Abildgaard[1], Michal Lubas[5], Jiri Bartek[1,6], Elena Papaleo[1,7] and Lisa B. Frankel [ID][1,5✉]

During autophagy, the coordinated actions of autophagosomes and lysosomes result in the controlled removal of damaged intracellular organelles and superfluous substrates. The evolutionary conservation of this process and its requirement for maintaining cellular homeostasis emphasizes the need to better dissect the pathways governing its molecular regulation. In our previously performed high-content screen, we assessed the effect of 1530 RNA-binding proteins on autophagy. Among the top regulators, we identified the eukaryotic translation initiation factor 4A-3 (eIF4A3). Here we show that depletion of eIF4A3 leads to a potent increase in autophagosome and lysosome biogenesis and an enhanced autophagic flux. This is mediated by the key autophagy transcription factor, TFEB, which becomes dephosphorylated and translocates from the cytoplasm to the nucleus where it elicits an integrated transcriptional response. We further identified an exon-skipping event in the transcript encoding for the direct TFEB kinase, GSK3B, which leads to a reduction in GSK3B expression and activity. Through analysis of TCGA data, we found a significant upregulation of eIF4A3 expression across several cancer types and confirmed the potential relevance of this newly identified signaling axis in human tumors. Hence, our data suggest a previously unrecognized role for eIF4A3 as a gatekeeper of autophagy through the control of TFEB activation, revealing a new mechanism for autophagy regulation.

INTRODUCTION

Macroautophagy (hereafter referred to as autophagy) is an evolutionarily conserved catabolic process that mediates degradation and recycling of intracellular components. Autophagy is constitutively active at low levels in most cells of the body, while it is potently induced in response to cellular stress, such as starvation, in order to promote nutrient recycling and clearance of superfluous material [1]. Defective autophagy and/or lysosomal function has been linked to a diverse group of diseases, including lysosomal storage disorders, neurodegenerative disorders, and cancer [2]. In the latter, a complicated interplay exists, in which the impact of autophagy is multifaceted and context-dependent. Autophagy can, in some instances, play a preventive role in early tumorigenesis through the maintenance of cellular homeostasis and protection of genome integrity. However, autophagy can contrarily fuel tumor growth and support the development of therapeutic resistance, by facilitating tumor cell survival and fitness through the generation of nutrients [3, 4].

The autophagy process is intricately controlled at multiple layers including the transcriptional level, where a number of transcription factors are responsible for initiating and sustaining the autophagic response [5, 6]. A key transcriptional regulator of

this pathway is transcription factor EB (TFEB), which belongs to the MiT-TFE family of helix–loop–helix transcription factors, including three additional members MITF, TFE3, and TFEC [7]. TFEB has been shown to bind to the promoter regions of multiple autophagy genes involved in different steps of the pathway, including autophagy initiation, membrane elongation, cargo capture, and autophagosome–lysosome fusion. In addition, TFEB regulates the expression of a large cohort of genes involved in lysosomal biogenesis and function [8–10]. As a result of this broad transcriptional response, essential for the cooperative function of both early and late steps of the pathway, TFEB mediates an integrated control of cellular clearance via the induction of autophagic flux. Its activity is largely controlled by its subcellular localization, which is in turn regulated by its phosphorylation status. Under basal conditions in nutrient-replete medium, phosphorylated TFEB is retained in the cytoplasm. Upon its activation, by e.g. nutrient starvation, TFEB is rapidly dephosphorylated and translocates to the nucleus where it binds to the promoters of target genes and induces the subsequent transcriptional response [11]. Phospho-proteomic studies have revealed several phosphorylation sites on TFEB, regulated by upstream kinases including AKT1, mammalian target of rapamycin, and glycogen synthase kinase 3 beta (GSK3B) [12–15].

[1]Danish Cancer Society Research Center, Copenhagen, Denmark. [2]Biodonostia Health Research Institute, San Sebastian, Spain. [3]Ikerbasque, Basque Foundation for Science, Bilbao, Spain. [4]The Francis Crick Institute, London, UK. [5]Biotech Research and Innovation Center, University of Copenhagen, Copenhagen, Denmark. [6]Department of Medical Biochemistry and Biophysics, Division of Genome Biology, Science for Life Laboratory, Karolinska Institute, Stockholm, Sweden. [7]Cancer Systems Biology, Section for Bioinformatics, Department of Health and Technology, Technical University of Denmark, Lyngby, Denmark. ✉email: frankel@cancer.dk
Edited by D. Rubinsztein

GSK3B-mediated phosphorylation of TFEB at S134 and S138 represents an initial event, permissive for TFEB's localization to the lysosome, where it is further phosphorylated by additional kinases, leading to its cytosolic retention. Hence, GSK3B inactivation potently induces autophagy through the loss of TFEB phosphorylation followed by its nuclear translocation [12].

In a previously performed high-throughput screen, we assayed the effects of 1530 RNA-binding proteins (RBPs) on autophagy [16]. Among the top hits, confirmed in a secondary validation screen, we identified the eukaryotic initiation factor 4A-3 (eIF4A3), as a potent regulator of autophagy. eIF4A3 is an Asp-Glu-Ala-Asp (DEAD) box-family adenosine triphosphate (ATP)-dependent RNA helicase, well known for its role as a core component of the exon junction complex (EJC), which mediates nonsense-mediated decay (NMD) [17, 18]. eIF4A3 has also been implicated in various aspects of RNA processing and function, including splicing, mRNA export, localization, and translation [19–24]. Perturbation of eIF4A3 expression affects numerous biological processes, including cell cycle regulation, apoptosis, and stress granule maintenance [25–27].

In this study, we provide evidence that eIF4A3 depletion leads to induction of both early and late steps in the autophagy pathway, resulting in an enhanced autophagic flux. Mechanistically, we show that this is caused by the broad transcriptional induction of autophagy- and lysosome-related genes and that a key mediator of this transcriptional response is TFEB. We demonstrate that, upon loss of eIF4A3, TFEB is de-phosphorylated and shuttles from the cytoplasm to the nucleus, in part due to the mis-splicing of its upstream kinase, GSK3B. Hence, our data suggest a previously unrecognized role for eIF4A3 as a gatekeeper of autophagy through the control TFEB activation. Our analysis of The Cancer Genome Atlas (TCGA) data from several tumor types further suggests an oncogenic role for eIF4A3 and implicates this signaling axis in human cancers.

RESULTS
eIF4A3 regulates autophagic flux
Intrigued by the steadily increasing evidence for several new and previously unrecognized functions of RBPs, we recently performed a high-throughput screen in search of RBPs involved in autophagy regulation [16]. Among the top identified autophagy-regulating candidates from the screen, we found the DEAD-box RNA helicase eIF4A3. Confirming the original screen findings, we used MCF-7 cells stably expressing the autophagy marker green fluorescent protein (GFP)-LC3B and observed that small interfering RNA (siRNA)-mediated depletion of eIF4A3 with two independent siRNAs (A and B) significantly increased the level of GFP-LC3B puncta (Fig. 1A–C). The knockdown efficiency of both siRNAs was confirmed at the protein and RNA levels (Fig. 1D, E). Since an accumulation of autophagosomes can either reflect their enhanced formation or a block in their degradation, we assessed autophagic flux by evaluating lysosome-induced cleavage of the GFP tag from the GFP-LC3B fusion protein [28]. For this purpose, we established autophagy-deficient ATG5 and ATG7 MCF-7 CRISPR-cas9 knockout (KO) cells and compared them to a non-targeting (scramble) CRISPR-cas9 control cell line (NTC) [4, 29, 30]. While total GFP-LC3B expression levels increased after eIF4A3 knockdown in all three cell lines, eIF4A3 depletion resulted in the appearance of a lysosome-induced GFP cleavage product in the NTC cells, indicative of enhanced autophagic flux, which was absent in the autophagy-deficient cell lines (Fig. 1F). This finding was substantiated by fluorescence microscopy, which similarly showed that the induction of GFP-LC3B puncta by eIF4A3 depletion was abrogated in the autophagy-deficient cells (Fig. 1G). Further supporting the increased number of autophagosomes seen after siRNA-mediated eIF4A3 depletion, endogenous LC3B presented at higher levels in its lipidated form (Fig. 1H). The

enhanced LC3B lipidation was further increased by Bafilomycin A1 treatment, additionally suggesting an effect on autophagic flux (Fig. S1A). Moreover, loss of eIF4A3 led to a reduction in the autophagic cargo protein p62, which also presented with a faster clearance rate after translational block by cycloheximide (CHX) treatment (Fig. S1A, B). Together, these data suggest that depletion of eIF4A3 induces autophagic flux in a manner dependent on the canonical autophagy machinery. The protein and mRNA levels of eIF4A3 itself remained unaffected in an 8-h time course of autophagy induction by Hank's Balanced Salt Solution (HBSS) or Torin-1 treatment, as well as in the presence of the lysosomal inhibitor, Bafilomycin A1 (Fig. S1C, D). These findings indicate that the eIF4A3 protein is neither a substrate for autophagy-mediated degradation nor is its transcription influenced by key autophagy-inducing stimuli.

eIF4A3 affects early and late autophagy-related vesicles
To investigate this phenotype in closer detail, we explored both early and late stages of the autophagy pathway. Immunofluorescent (IF) stains for the phagophore-associated protein WIPI2 revealed a significant increase in WIPI2 puncta in MCF-7 cells, suggesting that the early stages of autophagosome formation were enhanced upon loss of eIF4A3 (Fig. 2A–C). Likewise, by staining for the lysosomal marker, LAMP1, we confirmed a large increase in the level of lysosome-associated LAMP1 puncta, which were diffusely expressed throughout the cytoplasm (Fig. 2D–F). While overall levels of WIPI2 protein remained unaffected, total LAMP1 protein levels were also enhanced by eIF4A3 knockdown, as assessed by western blotting (Fig. S2A). By staining for eIF4A3 itself, we confirmed that key IF phenotypes co-occurred in the same cells as those displaying a strong eIF4A3 knockdown efficiency (Fig. S2B). Further investigation by transmission electron microscopy indicated an increased abundance of both autophagic vacuoles and lysosomes after eIF4A3 depletion, while the ultrastructure of these vesicles appeared normal, without any overt morphological alterations (Fig. 2G–J). Altogether, these data highlight a role for eIF4A3 as an inhibitor of the autophagy–lysosomal pathway. Upon eIF4A3 depletion, autophagosome and lysosome formation is enhanced, which is accompanied by increased autophagic flux in a manner dependent upon the canonical LC3 lipidation machinery.

Loss of eIF4A3 induces a broad autophagic–lysosomal transcriptional signature
eIF4A3 has been attributed several biological roles related to RNA homeostasis, including NMD, splicing, mRNA localization, and translation [19–24]. To assess for any potential effects of eIF4A3 on global translation in MCF-7 cells, we performed an assay using incorporation of fluorescently tagged O-propargyl-puromycin (OPP) into all newly translated proteins. We did not observe any effects of eIF4A3 depletion on global protein synthesis, in contrast to a short treatment with the translational inhibitor CHX (Fig. S3A). As the effect of eIF4A3 was seemingly unrelated to any major perturbation of global translation, we performed transcriptomic profiling by RNA sequencing (RNA-seq) of MCF-7 cells after eIF4A3 depletion with two independent siRNAs. By differential expression analysis using DEseq2 [31], we obtained an overview of significantly deregulated transcripts for each siRNA (fold change (FC) ≥2 and adjusted p value ≤0.05) (Fig. 3A, B). Comparison of the two siRNAs revealed a common overlap of 940 upregulated and 1233 downregulated transcripts (Fig. 3C). We performed gene ontology (GO) analysis for "Biological Process" and "Cellular Component" and the top ten enriched GO categories for upregulated or downregulated genes are shown in Fig. 3D and Fig. S3B, respectively. A striking pattern among the upregulated genes revealed that the first six of ten top enriched categories were directly related to autophagy or lysosome-associated genes
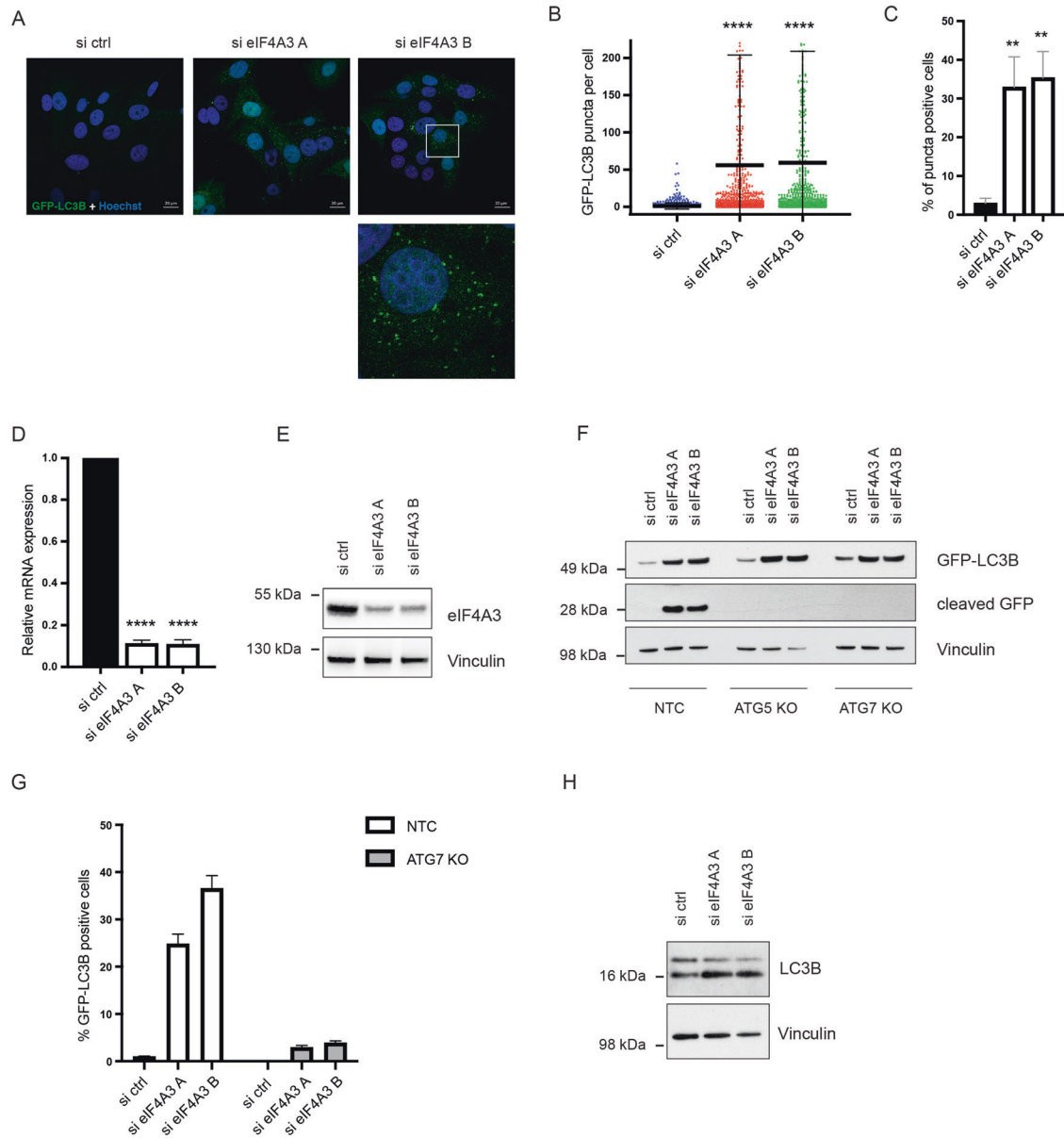
Fig. 1 eIF4A3 regulates autophagic flux. A Representative images of GFP-LC3B puncta in MCF-7 cells 72 h after transfection with ctrl and eIF4A3 siRNAs. Scale bars 20 μm. Enlargement of the boxed area shown below. **B** Scatter dot plots showing the number of GFP-LC3B puncta per cell in MCF-7 cells (**A**). Data are mean + standard deviation (SD) from three independent experiments. Values obtained from the quantification of >900 cells. ****$p < 0.0001$. Student's t test. **C** Quantification of GFP-LC3B-positive MCF-7 cells (**A**). Cells with >10 puncta were considered GFP-LC3B positive. Data are mean + SD from three independent experiments. Values obtained as above from the quantification of >900 cells. **$p < 0.01$, ****$p < 0.0001$. Student's t test. **D** Quantification of eIF4A3 knockdown efficiency of both siRNAs by qRT-PCR. Data are mean + SD from three independent experiments. ****$p < 0.0001$. Student's t test. **E** Western blot of MCF-7 GFP-LC3B cells after 72 h transfection with the indicated siRNAs. A representative experiment is shown ($n = 3$). **F** Representative western blot of GFP-LC3B and cleaved GFP in three MCF-7 GFP-LC3B CRISR/Cas9 cell lines: non-targeting control (NTC), ATG5 KO, and ATG7 KO cells. siRNA transfections as indicated for 72 h. A representative experiment is shown ($n = 3$). **G** Quantification of GFP-LC3B-positive cells in NTC and ATG7 KO cell lines from **F**. Cells with >10 puncta were considered GFP-LC3B positive. Data are mean + SD from three independent experiments. **H** Western blot of endogenous LC3B in MCF-7 GFP-LC3B cells after 72 h transfection with the indicated siRNAs. A representative experiment is shown ($n = 3$).

(Fig. 3D). Heatmaps displaying the FCs of transcripts pertaining to the top ten enriched GO categories or specifically focused on the six autophagy/lysosome-related categories are shown in Fig. S3C and Fig. 3E, respectively. Interestingly, among the 75 genes from Fig. 3E, we noted multiple known targets of the master autophagy/lysosome transcription factor TFEB. To validate the RNA-seq findings, we performed quantitative real-time PCR (qRT-PCR) focusing on 20 known TFEB targets identified in Fig. 3E, all for which we confirmed a clear upregulation after knockdown by

both siRNAs (Fig. 3F). Since eIF4A3 has been implicated in mRNA stability, we also investigated whether the stability of key TFEB targets was affected. By use of Actinomycin D chase analysis, we confirmed that the time-dependent decay of these transcripts after a transcriptional block remained unaffected by eIF4A3 siRNAs, in contrast to the eIF4A3 transcript itself (Fig. S3D). Taken together, this data reveals a novel interplay between eIF4A3 and an autophagy/lysosome transcriptional signature, including a large cohort of targets of the transcription factor TFEB.
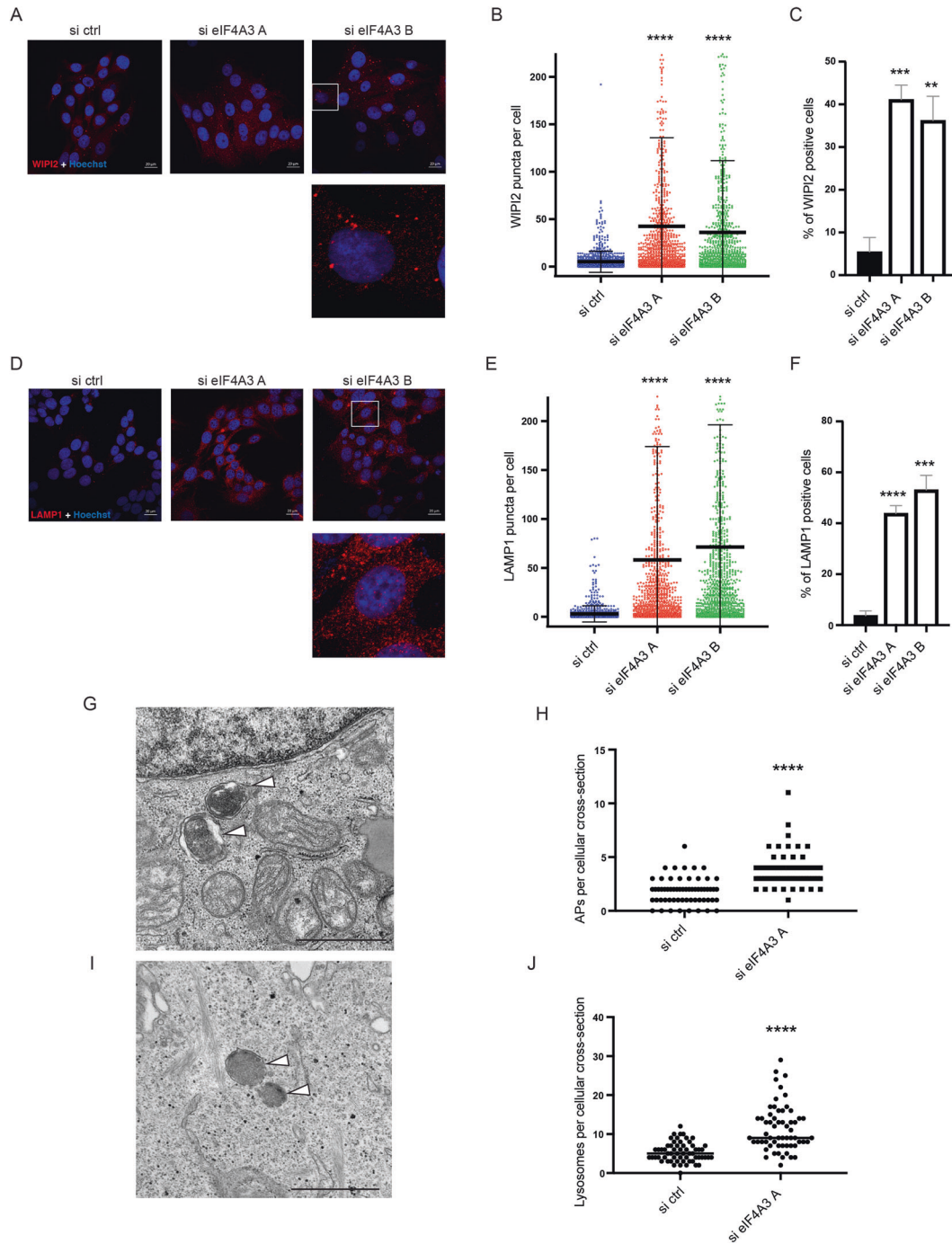
Fig. 2 eIF4A3 affects early and late autophagy-related vesicles. A Representative images of WIPI2 puncta in MCF-7 cells 72 h after transfection with ctrl and eIF4A3 siRNAs. Scale bars 20 μm. Enlargement of boxed area shown below. **B** Scatter dot plots showing the number of WIPI2 puncta per cell in MCF-7 cells (**A**). Data are mean + SD from three independent experiments. Values obtained from the quantification of >900 cells. ****$p < 0.0001$. Student's t test. **C** Quantification of WIPI2-positive MCF-7 cells (**A**). Cells with >20 puncta were considered WIPI2 positive. Data are mean + SD from three independent experiments. Values obtained as above from the quantification of >900 cells. **$p < 0.01$, ***$p < 0.001$. Student's t test. **D** Representative images of LAMP1 puncta in MCF-7 cells 72 h after transfection with ctrl and eIF4A3 siRNAs. Scale bars 20 μm. Enlargement of boxed area shown below. **E** Scatter dot plots showing the number of LAMP1 puncta per cell in MCF-7 cells (**D**). Data are mean + SD from three independent experiments. Values obtained from the quantification of >900 cells. ****$p < 0.0001$. Student's t test. **F** Quantification of LAMP1-positive MCF-7 cells (**D**). Cells with >20 puncta were considered LAMP1 positive. Data are mean + SD from three independent experiments. Values obtained as above from the quantification of >900 cells. ***$p < 0.001$, ****$p < 0.0001$. Student's t test. **G** Transmission electron microscopic (TEM) images from MCF-7 GFP-LC3 cells after 72 h transfection. Arrowheads indicate autophagic vacuoles. Scale bars 1 μm. **H** Quantification of autophagosomes per cellular cross-section corresponding to **G**. Data are mean + standard error of the mean (SEM) ($n = 2$) (30–35 cells/sample). ****$p < 0.0001$. Student's t test. **I** Transmission electron microscopic (TEM) images from MCF-7 GFP-LC3 cells after 72 h transfection. Arrowheads indicate lysosomes. Scale bars 1 μm. **J** Quantification of lysosomes per cellular cross-section corresponding to **I**. Data are mean + standard error of the mean (SEM) ($n = 2$) (30–35 cells/sample). ****$p < 0.0001$. Student's t test.
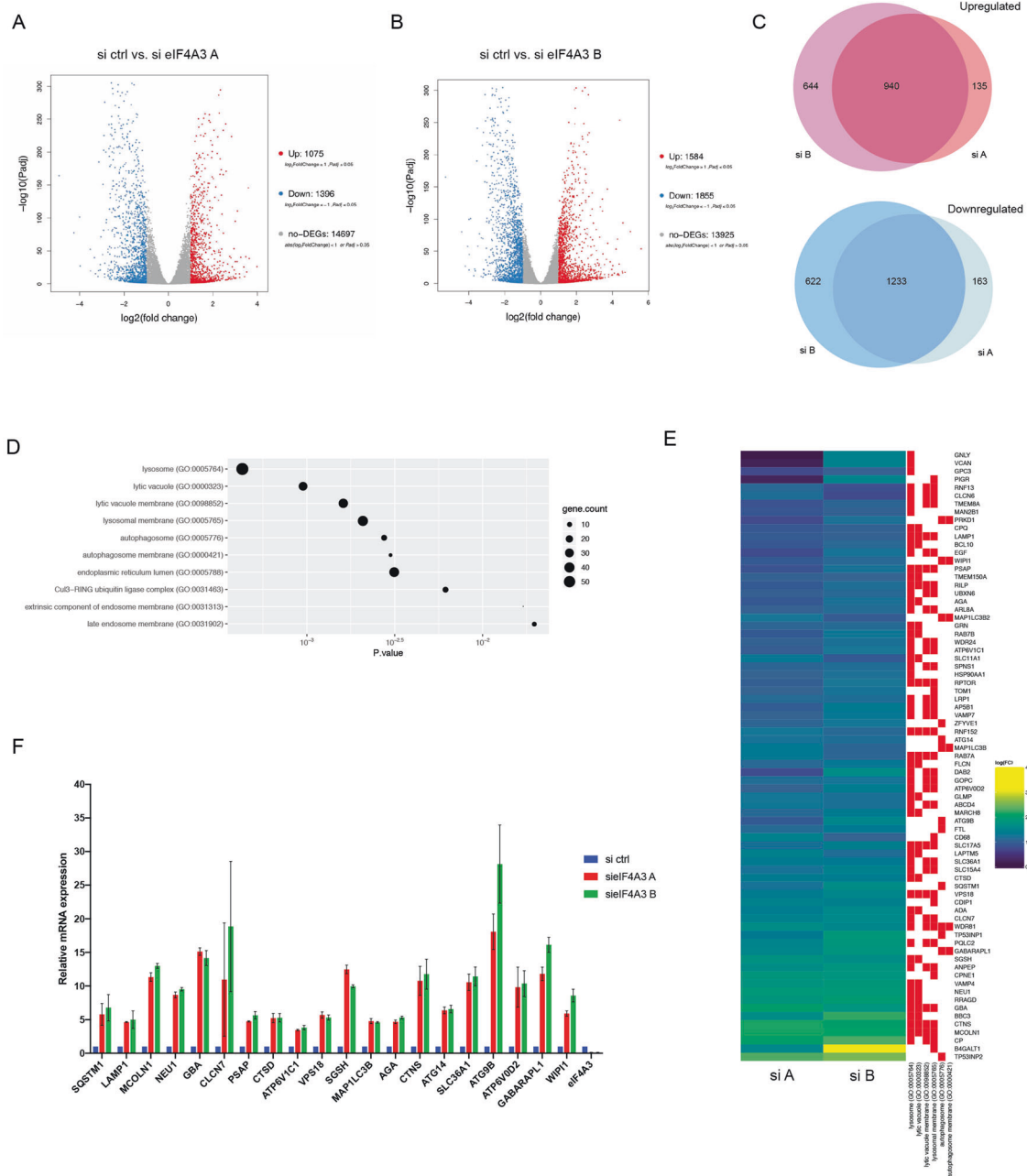
Fig. 3 eIF4A3 regulates an integrated autophagy and lysosomal transcriptional response. A, B Volcano plots displaying significantly upregulated and downregulated transcripts after 72 h transfection with si eIF4A3 A or si eIF4A3 B relative to si ctrl in MCF-7 eGFP-LC3B cells. Differentially expressed genes are denoted in blue or red, applying cut-offs of fold change ≥2 and adjusted p value ≤0.05. **C** Venn diagrams displaying the amount of common or unique significantly upregulated and downregulated transcripts between si eIF4A3 A vs. si eIF4A3 B from the RNA-seq analysis (**A, B**). **D** Dot plot displaying the top 10 significantly enriched GO categories for cellular compartment among upregulated transcripts for both si eIF4A3 A and si eIF4A3 B. **E** Heatmap of transcripts from all autophagy- and lysosome-related categories of **D. F** qRT-PCR validation of TFEB target mRNAs identified in **E**. Experiments performed under same conditions as the RNA-seq with the indicated siRNAs. Data represent the mean + SD from three independent experiments.

eIF4A3 affects TFEB phosphorylation and intracellular localization

Prompted by the large number of TFEB targets identified from our RNA-seq analysis, we further investigated a potential role for TFEB in the eIF4A3-mediated transcriptional response. Interestingly, we found that endogenous TFEB displayed a clear downward shift by western blotting in response to eIF4A3 knockdown in MCF-7 cells (Fig. 4A). Besides MCF-7 cells, analysis of HEK 293, HCT116, and U2OS cells revealed a similar shift, confirming the broader relevance of this phenotype across cell types (Fig. 4B). It is well

established that, upon autophagy induction, an electrophoretic migration shift of TFEB due to its de-phosphorylation leads to its subsequent translocation to the nucleus [11]. In line with this, we observed a clear reduction in the level of phosphorylated TFEB after eIF4A3 knockdown (Fig. S4A). We next analyzed TFEB's intracellular localization by IF and confirmed an increase in the abundance of nuclear localized endogenous TFEB after depletion of eIF4A3 (Fig. 4C, D). This observation was confirmed with a GFP-tagged TFEB, which also clearly translocated from the cytoplasm to the nucleus upon eIF4A3 knockdown (Fig. 4E and Fig. S4B).
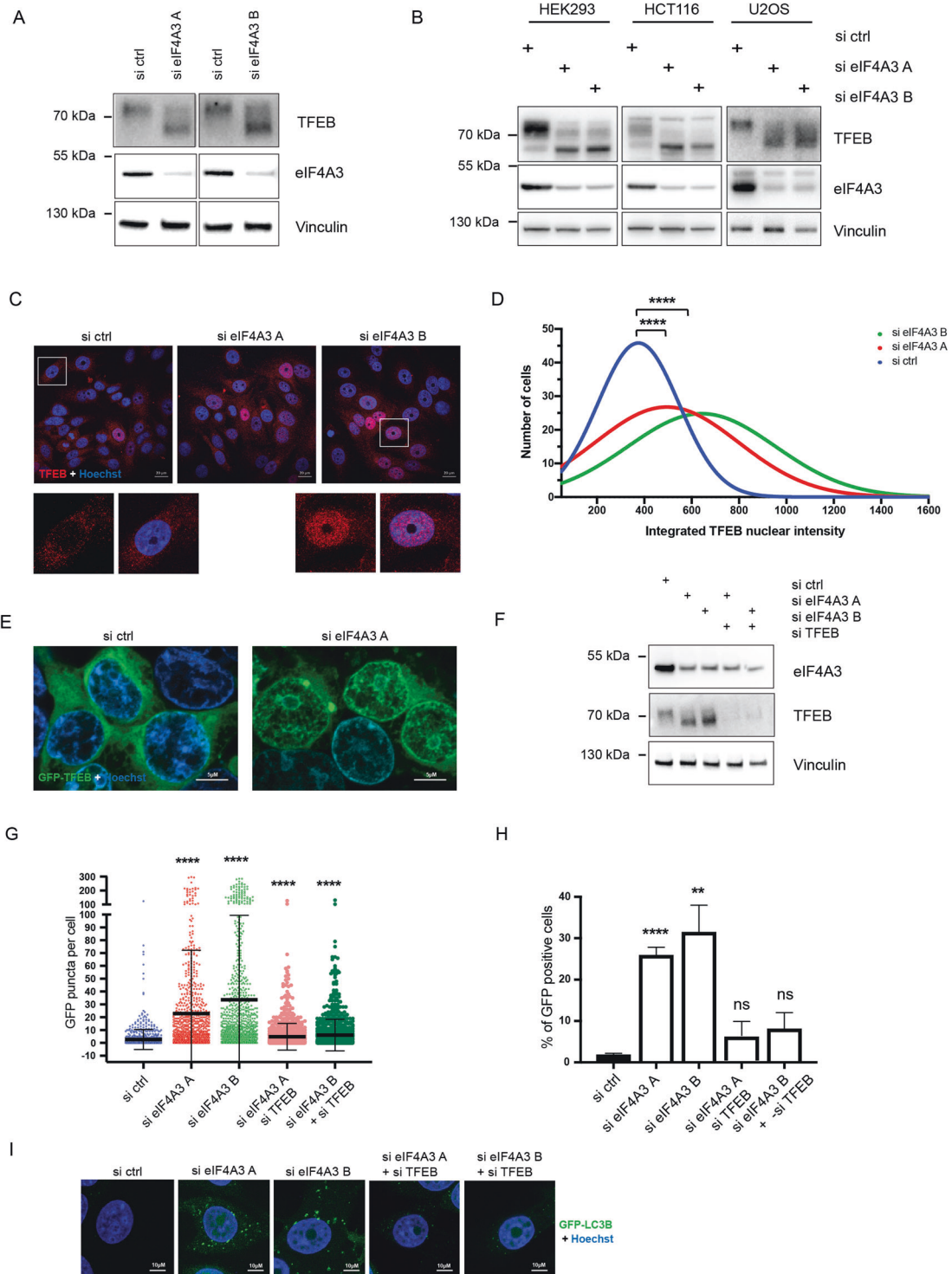
Fig. 4 Nuclear re-localization of TFEB in response to eIF4A3 depletion. A Western blot of TFEB and eIF4A3 in MCF-7 GFP-LC3B cells after 72 h transfection with the indicated siRNAs. A representative experiment is shown ($n = 3$). **B** Western blot of TFEB and eIF4A3 in HEK293, HCT116, and U2OS after 48–72 h transfection with the indicated siRNAs. Representative experiments for each cell line are shown ($n = 3$). **C** Representative images of endogenous TFEB immunofluorescence in MCF-7 GFP-LC3B cells 72 h after transfection with ctrl and eIF4A3 siRNAs. Scale bars 20 μm. **D** Gaussian distribution of TFEB intensity in nucleus (**C**). Data represent three independent experiments. Values obtained from the quantification of >900 cells. ****$p < 0.0001$. Student's t test. **E** Representative images of HEK cells transiently transfected with GFP-TFEB (48 h) together with the indicated combinations of siRNAs (72 h). Scale bars 5 μm. **F** Western blot of TFEB and eIF4A3 in MCF-7 GFP-LC3B cells after 72 h transfection with the indicated combinations of siRNAs. A representative experiment is shown ($n = 3$). **G** Scatter dot plots showing the number of GFP-LC3B puncta per cell in MCF-7 GFP-LC3B cells after transfection with the indicated siRNAs. Data are mean + SD from three independent experiments. Values obtained from the quantification of >900 cells. ****$p < 0.0001$. Student's t test. **H** Quantification of GFP-LC3B-positive cells related to **F**, **G**. Cells with >20 puncta were considered GFP-LC3B positive. Data are mean + SD from three independent experiments. **$p < 0.01$, ****$p < 0.0001$, ns; not significant. Student's t test. **I** Representative images of GFP-LC3B puncta in MCF-7 GFP-LC3B cells 72 h after transfection with the indicated siRNAs related to **F–H**. Scale bars 10 μm.

Both the shift in TFEB electrophoretic migration and its increased nuclear localization clearly resemble the effects of a short starvation treatment with HBSS (Fig. S4C–E), a well-known inducer of autophagy, causing TFEB de-phosphorylation and cytoplasmic-to-nucleus translocation [9]. The specificity of the TFEB antibody for IF was confirmed by its siRNA-mediated knockdown (Fig. S4C–E). To verify the importance of TFEB for eIF4A3-mediated regulation of autophagy, we co-depleted TFEB and eIF4A3 and confirmed their individual and combined knockdown efficiencies by western blot (Fig. 4F). Importantly, co-depletion of eIF4A3 and TFEB significantly impaired the induction of GFP-LC3B puncta, suggesting clear dependency on TFEB for eIF4A3-mediated regulation of autophagy (Fig. 4G–I).

Phenotypic rescue by reconstitution of eIF4A3
To further verify the role of eIF4A3 in mediating the observed phenotypes, we created MCF-7 GFP-LC3B cells with doxycycline-inducible expression of eIF4A3, which led to a reduction in LC3B lipidation levels as well as some reduction in total LC3B (Fig. 5A and Fig. S5A). Using this cell line, we effectively re-expressed eIF4A3 in an eIF4A3-depleted background, to levels similar to that of baseline in control cells, and notably, this reconstitution blocked the shift of TFEB caused by both siRNAs (Fig. 5B). Moreover, the doxycycline-induced re-expression of eIF4A3 significantly abrogated the nuclear translocation of TFEB (Fig. 5C, D) and dampened the effects on GFP-LC3B, WIPI2, and LAMP1 puncta (Fig. 5E, F). The data therefore indicate that reconstitution of eIF4A3 is sufficient to block TFEB nuclear translocation, resulting in a phenotypic rescue at both early and late steps of the autophagy pathway. Of note, eIF4A3 overexpression on its own did not impact TFEB localization in conditions of low basal autophagy, in which there is a limited window for observing any further effect (Fig. 5D). However, in conditions of induced autophagy by Torin1 treatment, eIF4A3 upregulation significantly decreased both GFP-LC3B puncta and the extent of TFEB nuclear localization (Fig. S5B–E), as well as LC3B lipidation (Fig. 5A), demonstrating a functional impact of eIF4A3 upregulation on TFEB and autophagy.

Exon skipping in GSK3B contributes to loss of TFEB phosphorylation
To further uncover the mechanism behind eIF4A3-mediated cytoplasmic-to-nuclear shuttling of TFEB, we performed a transcriptome-wide analysis of alternative splicing events using the RNA-seq data from MCF-7 cells after eIF4A3 depletion. Applying rMATS [32] to identify differential splicing events, we found that eIF4A3 was broadly implicated in multiple types of splice event (Fig. 6A). Focusing on the predominant event of exon skipping, for which eIF4A3 has a previously established role [23, 24], we applied a cut-off of false discovery rate (FDR) <0.01 leading to the identification of 2065 skipped exon (SE) events in 1292 genes for si A vs. si CTRL and 2644 SE events in 1600 genes for si B vs. si CTRL (Fig. 6B and Table S3). Of these events, we found 1675 events within 1080 genes common to both siRNAs (Table S3). Considering the loss in TFEB phosphorylation, we asked whether inactivation of a kinase that phosphorylates TFEB may contribute to this phenotype by overlaying these 1080 common genes with a list of 517 known kinases [33]. Among 44 kinases subjected to exon-skipping events, we found one kinase, GSK3B, known to phosphorylate TFEB [12] (Table S3 and Fig. 6C). Further analysis of the GSK3B transcript showed that, upon eIF4A3 depletion, both exons 6 and 7 are skipped (Fig. 6D). To confirm the skipping of these two exons, we performed RT-PCR using primers placed within exons 5 and 8, respectively. Besides yielding a full-length band of expected size (360 bp) in all samples, a shorter product of approximately 150 bp was present specifically in the eIF4A3-depleted samples, corresponding in length to the product of expected size when exons 6 and 7 are skipped (Fig. 6E). We further validated this exon-skipping event by qRT-PCR using a primer

spanning the exon 5–8 junction, which resulted in the specific amplification of a product only after eIF4A3 knockdown, while regions of GSK3B further upstream or downstream of the skipped exons remained unaffected (Fig. 6F). While a minor decrease in the full-length GSK3B transcript is apparent in Fig. 6E, we confirmed this in a more quantitative manner by qRT-PCR, which indicated a reduction in the full-length GSK3B transcript (Fig. S6A). Importantly, this resulted in a concordant reduction of GSK3B protein levels, as well as decreased activity of GSK3B toward its known substrates, IkBα and β-catenin (Fig. S6B–D).

GSK3B-mediated phosphorylation of TFEB represents an initial event that allows for TFEB's subsequent phosphorylation by additional kinases, all contributing to its cytoplasmic retention [12]. Hence, we hypothesized that even a mild defect in GSK3B, caused by exon skipping in small fraction of transcripts, may be of functional importance for the observed phenotypes. To test this, we co-expressed an active form of correctly spliced GSK3B from a cDNA together with eIF4A3 or ctrl siRNAs. Interestingly, we found that GSK3B could inhibit the si-eIF4A3-induced TFEB shift relative to the empty vector (Fig. 6G). In addition, GSK3B expression significantly blocked the nuclear localization of TFEB and instead led to its accumulation in cytosolic perinuclear areas, which likely represent lysosomes (Fig. 6H, I). These data suggest the potential functional requirement for GSK3B kinase activity for the autophagy-related phenotypes.

eIF4A3 is deregulated in multiple cancers and shows correlative trends with TFEB targets
To assess the potential importance of the identified eIF4A3–TFEB signaling axis human cancers, we analyzed eIF4A3 expression levels across 18 cancer types using transcriptomics data from TCGA. Interestingly, this revealed a significant deregulation of eIF4A3 expression levels in 14 of the 18 cancer types (78%) relative to corresponding normal tissue samples (Fig. 7A). In all cases except for one (KICH), eIF4A3 was upregulated. Focusing our analysis on cancer types displaying the strongest upregulation of eIF4A3 (logFC >0.5), which included COAD, READ, GBM, ESCA, BRCA, LUSC, and LUAD, we performed a spearman correlation analysis to assess for correlations in the expression levels between eIF4A3 and a list of confirmed TFEB targets compiled from the literature (Table S2) [8–10]. Despite the high complexity within analyzed tumors and an established heterogeneity of the TFEB response across tissue types, this analysis revealed a cluster of TFEB targets displaying a consistent negative expression correlation with eIF4A3 across all cancer types, including key transcripts also validated from our RNA-seq data such as GABARAPL1, CLCN7, LAMP1, and PSAP (Fig. 7B). Further analysis at the cancer subtype level, for those subtypes meeting sample number criteria (see "Methods"), also revealed a cluster of TFEB targets with negative expression correlation to eIF4A3 (Fig. 7C). Hence, these data are consistent with the existence an eIF4A3–TFEB signaling axis across several cancers in which eIF4A3 is upregulated.

DISCUSSION
Our understanding of the molecular regulation of autophagy is quickly expanding along with the growing realization that this complex process is carefully controlled at multiple levels. The regulation of autophagy at the post-transcriptional level by RBPs is an understudied, yet emerging area [34]. Recent examples of RBPs implicated in post-transcriptional control of autophagy include the Pat1-Lsm7 complex, which stabilizes a subset of Atg mRNAs through protection from exosome-mediated 3′–5′ degradation during starvation in yeast [35]. Likewise, the cleavage and polyadenylation complex can promote the stability and expression of selected Atg mRNAs by mediating 3′-untranslated region elongation or starvation-induced alternative splicing [36]. The
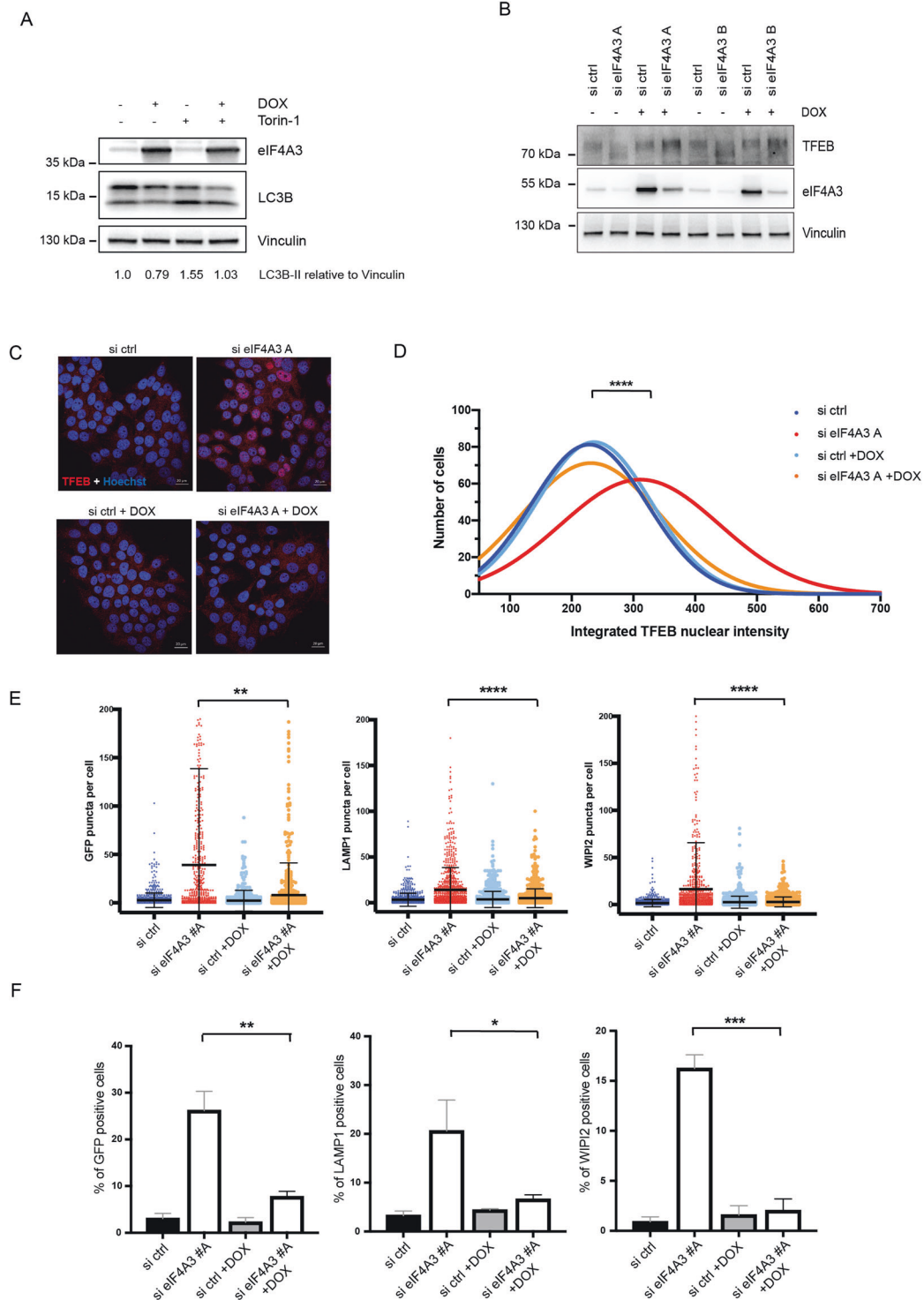
Fig. 5 Re-expression of eIF4A3 rescues all TFEB-related phenotypes. A Western blot showing the effects of inducible expression of pLVX eIF4A3 in MCF-7 GFP-LC3B cells (100 ng/ml doxycycline, 72 h) on endogenous LC3B levels in the presence or absence of autophagy induction by treatment with Torin1 (250 μM, 2 h). Representative experiment is shown ($n = 3$). Quantification of LC3B-II band intensity relative to Vinculin is shown below the figure. **B** Western blot in MCF-7 eGFP LC3B pLVX eIF4A3 cells with the indicated siRNA transfections (72 h) and doxycycline treatment (100 ng/ml doxycycline, 72 h). Representative experiment is shown ($n = 3$). **C** Representative images of endogenous TFEB immunofluorescence in the inducible system described in **A, B**. Scale bars 20 μm. **D** Gaussian distribution of TFEB intensity in the nucleus, related to **C**. Data represent three independent experiments. Values obtained from the quantification of >900 cells. ****$p < 0.0001$. Student's t test comparing si eIF4A3 A vs. si eIF4A3 A + DOX. **E** Scatter dot plots showing the number of GFP-LC3B, LAMP1, and WIPI2 puncta per cell in MCF-7 GFP-LC3B inducible system (**A**). Data are mean + SD from three independent experiments. Values obtained from the quantification of >900 cells. **$p < 0.01$, ****$p < 0.0001$. Student's t test. **F** Quantification of GFP-LC3B, LAMP1, and WIPI2-positive cells related to **E**. Cells with >20 puncta were considered GFP-LC3B, LAMP1, or WIPI2 positive, respectively. Data are mean + SD from three independent experiments. *$p < 0.05$, **$p < 0.01$, ***$p < 0.001$. Student's t test.
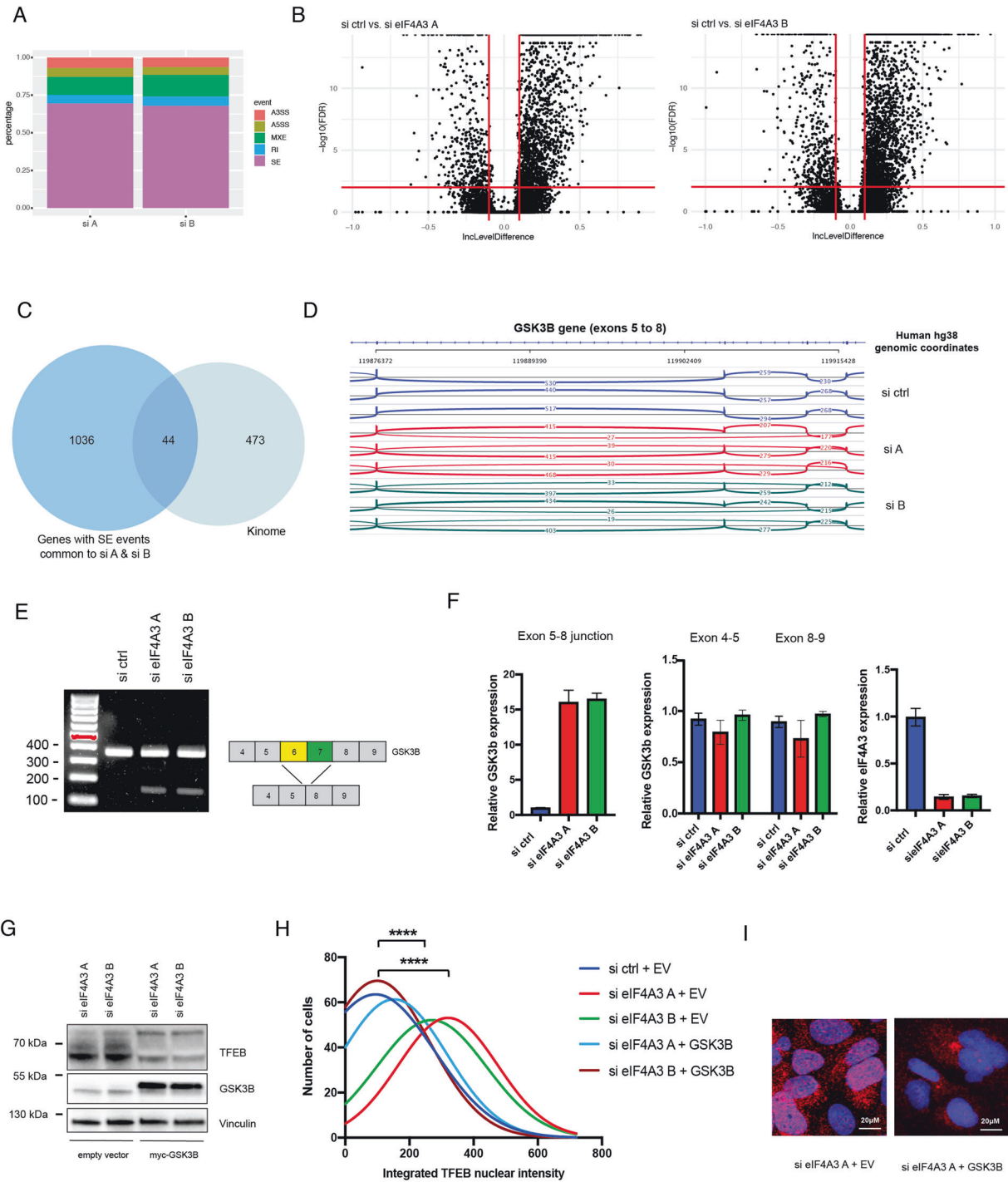
spliceosome factor, pre-mRNA processing factor 8, has been shown to enable correct splicing of the *ULK1* transcript during hypoxia [37]. Other RBPs have been shown to regulate autophagy translationally, including eIF5A, previously shown by us and others to assist the translation of key autophagy mRNAs, such as *ATG3* and *TFEB* [16, 38].

In this study, we reveal a novel function for the core EJC member, eIF4A3, through its unique control of an integrated autophagy and lysosomal transcriptional response. Originally identified in a high-throughput screen for RBP regulators of autophagy [16], we here show that depletion of eIF4A3 increases the cytoplasmic pool of autophagosomes and lysosomes, leading

to an increased autophagic flux, which is dependent on canonical autophagy machinery. This phenotype is mediated via a broad transcriptional induction of genes required for autophagy and lysosomal biogenesis, among which several are direct targets of the key transcription factor TFEB. Further investigation of the role of TFEB revealed the requirement for its de-phosphorylation and migration to the nucleus in mediating this autophagy induction. Mechanistically, we found that, upon knockdown of eIF4A3, an exon-skipping event in the TFEB kinase GSK3B, contributes to TFEB activation, which is importantly rescued by re-constitution of eIF4A3 or a correctly spliced GSK3B. Hence, we here describe a newly identified eIF4A3–GSK3B–TFEB signaling axis and

Fig. 6 eIF4A3 depletion causes exon skipping in GSK3B, which contributes to TFEB regulation. A Bar graph comparing proportions of significant number of splicing events (with |deltaPSI| > 0.1 and FDR < 0.01) in MCF-7 cells after eIF4A3 depletion with two independent siRNAs (A and B). Candidate alternative splicing events include exon skipping (SE), alternative 5′ (A5SS) and 3′ (A3SS) splice sites, mutually exclusive exons (MXE), and retained introns (RI). **B** Volcano plots showing changes in percentage spliced-in (PSI) and rMATS-computed Benjamini–Hochberg False Discovery Rate (FDR) of exons in MCF-7 cells after eIF4A3 depletion with two independent siRNAs A and B compared to cells transfected with siRNA ctrl (n = 3 biological replicates per sample). Exons with significant changes (|deltaPSI| > 0.1 and FDR < 0.01) are top and right/left to the cut-off lines labeled in red, respectively. **C** Venn diagram displaying overlap between genes subjected to exon-skipping events (common between si A and si B) and the human kinome. **D** Sashimi plot depicting the splice junction track for exons 5–8 in GSK3B gene and in MCF-7 cells treated with siRNA ctrl (top) or after eIF4A3 depletion with two independent siRNAs A (middle) and B (bottom). Splicing junctions predict the skipping of exons 6 and 7 in GSK3B mRNA. The hg38 reference human genome is shown above with exons displayed as solid blocks connected by thin lines representing introns. **E** Left: RT-PCR from MCF-7 cells transfected as indicated for 72 h followed by gel electrophoresis. Primers placed in exons 5 and 8 allow detection of full-length product (360 bp) as well as exon 6- and 7-skipped product (150 bp). Representative experiment is shown (n = 3). Right: schematic depiction of exon skipping in GSK3B after knockdown of eIF4A3. **F** qRT-PCR from MCF-7 cells transfected with the indicated siRNAs for 72 h. Primers used for GSK3B detection are indicated above graphs, detecting either the exon-skipped product (primer spanning exon 5–8 junction) (left) or regions upstream (exons 4–5) and downstream (exons 8–9) of exon skipping in GSK3B transcript (middle). Primers for detection of eIF4A3 used to confirm knockdown (right). All data are mean + SD from three independent experiments. **G** Western blot of transiently transfected U2OS cells with myc-GSK3B or corresponding empty vector control (36 h) and indicated siRNAs (48 h). Representative blot is shown (n = 3). **H** Gaussian distribution of TFEB intensity in the nucleus of U2OS cells transfected as in **G**. Data represent three independent experiments. Values obtained from the quantification of >900 cells. ****p < 0.0001. Student's t test compares si eIF4A3 A + EV (empty vector) vs. si eIF4A3 A + GSK3B and si eIF4A3 B + EV vs. si eIF4A3 B + GSK3B. **I** Representative images from **H**.

demonstrate its importance in regulating the TFEB-mediated transcriptional response.

Surprisingly, a relatively mild splicing defect of GSK3B contributes to a prominent de-phosphorylation of TFEB. Yet, we do not expect a linear relationship between these events, since GSK3B-mediated phosphorylation of TFEB serves as an initial permissive event, allowing for TFEB's subsequent lysosomal localization, where it is further phosphorylated by additional kinases [12]. Hence, even a mild reduction of GSK3B kinase can result in an amplified effect due to the subsequent loss of additional phosphorylations. Moreover, although GSK3B mis-splicing may play a role, it is likely that additional events may contribute here. For instance, the lysosomal calcium channel mucolipin 1, a direct TFEB target that is potently induced after eIF4A3 depletion (Fig. 3E, F), plays an important role in the activation of the major TFEB phosphatase, calcineurin [39]. This suggests the possibility of a positive feedback loop that could maintain or enhance the response through sustaining de-phosphorylation of TFEB. Moreover, the fact that the autophagy- and lysosome-related genes induced by eIF4A3 depletion also include non-TFEB targets emphasizes the complexity of this response, which is likely influenced by additional factors. Finally, splicing defects in additional genes including other kinases, though none of which target TFEB directly, may contribute through secondary or indirect effects.

Our analysis of TCGA data indicated a broadly consistent upregulation of eIF4A3 across several cancer types. Interestingly, we found that a cohort of TFEB targets inversely correlated with eIF4A3 expression, suggesting the potential importance of this signaling axis in tumors. However, the physiological significance of this finding and whether it represents a driving factor for tumorigenesis remains to be explored. Recent compound screens have led to the discovery of highly selective small-molecule inhibitors of eIF4A3 [40–43]. The demonstration of their suitability for in vivo studies, in which they have been shown to exhibit antitumor activity in a xenograft mouse model for colorectal cancer [42], opens the possibility for further exploring the potential for targeting eIF4A3 in vivo as a means of altering the autophagy/lysosomal response. TFEB overexpression alone can enhance clearance of bulk autophagy substrates such as long-lived proteins, lipid droplets, and damaged mitochondria [9, 44, 45]. An interest in therapeutically enhancing TFEB activation through targeting eIF4A3 may extend to other fields such as neurodegeneration, where it has been shown using various rodent models that TFEB activation is sufficient to alleviate pathogenic phenotypes in diseases associated with protein aggregation and/or lysosomal dysfunction [46–48].

Collectively, our study provides an important example of how an RBP, through its ability to safeguard splicing, acts as a gatekeeper of autophagy by maintaining its low basal levels through the cytoplasmic retention of TFEB. Upon loss of eIF4A3, the shuttling of TFEB to the nucleus stimulates an integrated transcriptional response in order to induce both early and late steps of the autophagic response. As eIF4A3 overexpression is a common event in several cancers, further exploration of this pathway will shed light on how autophagy and lysosome dysfunction, as well as perturbed cellular homeostasis, are implicated in tumorigenesis.

MATERIALS AND METHODS
Cell lines
MCF-7 GFP-LC3B parental and derived cell lines were propagated in RPMI 1640 (Invitrogen) supplemented with 6% fetal bovine serum (FBS) and 100 U/ml penicillin and 100 mg/ml streptomycin (P/S). MCF-7 eGFP-LC3B NTC, MCF-7 eGFP-LC3B ATG5 KO, and MCF-7 eGFP-LC3B ATG7 KO are described previously [4, 29]. MCF-7 GFP-LC3B cells expressing doxycycline-inducible pLVX eIF4A3 or pLVX empty control were generated by lentiviral transduction, as previously [30]. HEK 293, HCT116, and U2OS were propagated in DMEM supplemented with 10% FBS and P/S. The majority of experiments were performed in MCF-7 cells; however, due to lower transfection efficiency of plasmids in this cell line, experiments requiring plasmid transfections were performed in HEK 293 or U2OS.

Constructs and oligos
The pLVX-eIF4A3 plasmid was constructed with the NEBuilder HiFi DNA Assembly Kit (NEB, E2621), as described by the manufacturer, using the pcDNA 3.1-eIF4A3 plasmid as a template. Oligo sequences used for cloning are listed in Table S1. The TFEB plasmid was CMV-Sigma14-TFEB-GFP and GSK3B rescue experiments were performed with Tag5Amyc-GSK3b CA (Addgene plasmid # 16261). Corresponding empty vectors were used as controls.

Antibodies
Primary antibodies used for IF were LAMP-1 (H4A1) (Santa Cruz, sc-20011); WIPI2 (AbD Serotec MCA5780GA); TFEB (Cell Signaling, 4240S), eIF4A3 (Proteintech, 17504-1-AP). Primary antibodies used for immunoblotting were LC3B (Cell Signaling Technology, 2775); eIF4A3 (Proteintech, 17504-1-AP); GFP (Santa Cruz, sc-9996); LAMP-1 (H4A1) (Santa Cruz, sc-20011); WIPI2 (AbD Serotec MCA5780GA); TFEB (Cell Signaling Technology, 4240S); phospho-TFEB (Ser138) (provided by Andrea Ballabio); p62 (MBL International, PM045); Vinculin (Sigma, V9131); GSK3B (Santa Cruz E-11, sc-377213); IκBα (Cell Signaling, 9242); phospho-IκBα (Ser32) (Cell Signaling, 2859p); β-Catenin (Transduction Laboratories, 610153); phospho-β-Catenin (Ser33/37/Thr41) (Cell Signaling Technology, 9561S).
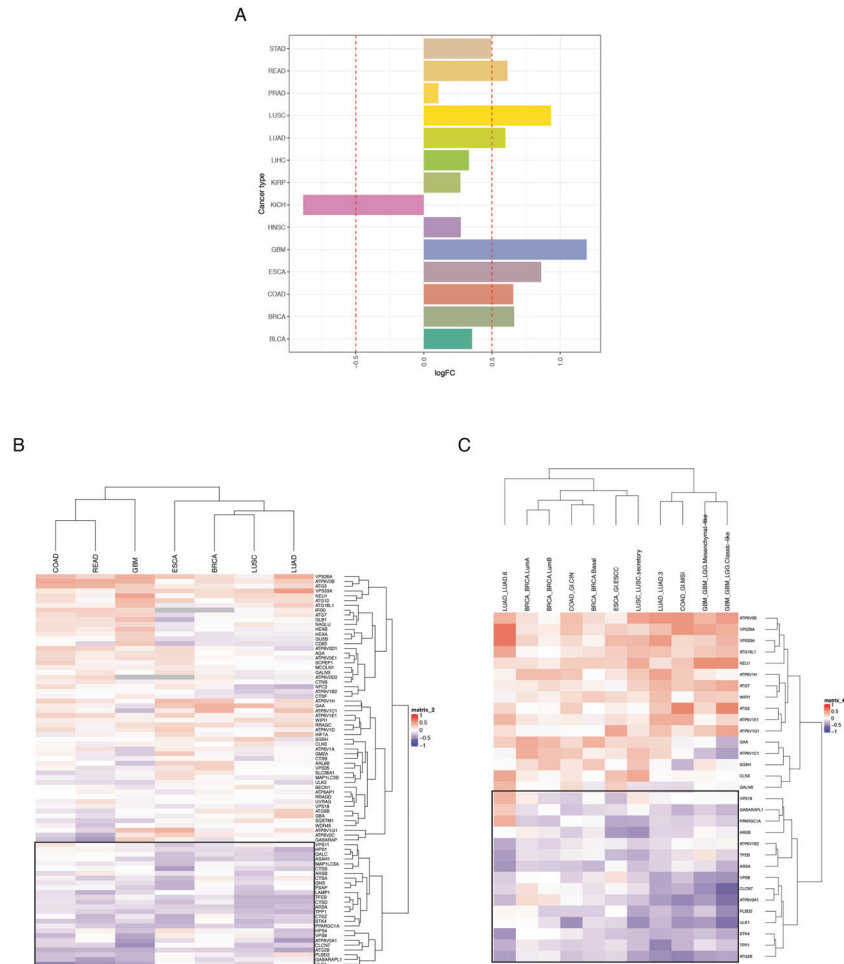
Fig. 7 eIF4A3 is deregulated in several cancers and shows expression correlation with TFEB targets. A Differential expression of eIF4A3 between primary tumor and normal tissue across 14 cancer types from TCGA data. Cancer types: STAD (stomach adenocarcinoma), READ (rectum adenocarcinoma), PRAD (prostate adenocarcinoma), LUSC (lung squamous cell carcinoma), LUAD (lung adenocarcinoma), LIHC (liver hepatocellular carcinoma), KIRP (kidney renal clear cell carcinoma), KICH (kidney chromophobe), HNSC (head and neck squamous cell carcinoma), GBM (glioblastoma multiforme), ESCA (esophageal carcinoma), COAD (colon adenocarcinoma), BRCA (breast invasive carcinoma), BLCA (bladder urothelial carcinoma). **B** Correlation between the expression profiles of eIF4A3 and TFEB targets performed on cancer types for which eIF4A3 is upregulated (logFC > 0.5). Hierarchical clustering was performed both on genes and cancer types. Boxed area highlights clusters of negative expression correlations. **C** as **B**, performed on cancer subtypes and after filtering as reported in "Methods." Boxed area highlights clusters of negative expression correlations.

IF microscopy
Cells grown on glass coverslips were washed twice in phosphate-buffered saline (PBS) and fixed in 4% (v/v) formaldehyde for 10 min at room temperature (RT) or 100% methanol for 3 min at −20 °C. Formaldehyde was washed off with PBS 3×. Cells were permeabilized with 0.1–0.2% (v/v) Triton X-100 in PBS for 5–10 min and incubated with blocking solution (DMEM/5% FBS/0.05% sodium azide or PBS/3% bovine serum albumin (BSA)) for 30 min at RT. Primary antibodies were diluted in blocking solution and added to the cells for overnight incubation at 4 °C. The next day, cells were washed twice with PBS–0.1% Tween20 and incubated with secondary antibodies conjugated with Alexa Fluor for 1 h at RT. Antibodies were washed off with PBS/0.1% Tween. Nuclei were stained with Hoechst 33342 diluted 1:2000 in PBS (Invitrogen, 11534886) for 10 min at RT. Samples on coverslips were mounted onto slides with Fluorescence mounting medium (Dako, S3023) and visualized by confocal microscopy (LSM 700, Carl Zeiss). A minimum of 10 pictures were taken per sample (counting >300 cells per sample/experiment), and fluorescent quantification and analysis of acquired images was performed using the automated image analysis software Cell Profiler 3.1.8.

Immunoblotting
Cell were lysed in RIPA buffer (150 mM NaCl, 1.0% IGEPAL® CA-630, 0.5% sodium deoxycholate, 0.1% sodium dodecyl sulfate (SDS), and 50 mM Tris,

pH 8.0) supplemented with protease and phosphatase inhibitors (Protease Inhibitor Cocktail, Sigma-Aldrich and Halt™ Phosphatase Inhibitor Cocktail, Thermo Scientific) and denatured for 10 min at 70 °C. Proteins were separated by SDS-Page electrophoresis, using 4–15% Tris-Glycine Mini-PROTEAN® TGX Stain-Free™ Protein Gels (Bio-Rad), or 10% acrylamide gels. Proteins were transferred to polyvinylidene difluoride membrane by semidry transfer or wet transfer and blocked in 5% non-fat dry milk or BSA in PBS–0.1% Tween. Membranes were incubated with primary antibodies overnight at 4 °C and secondary antibodies for 1 h at RT. The signal was visualized with Amersham ECL Western Blotting Detection Reagent (GE Healthcare) in an Amersham imager 600 (GE Healthcare).

Transmission electron microscopy
After 72 h transfection, the MCF-7 GFP-LC3B cells were fixed in 2% v/v glutaraldehyde in 0.05 M sodium phosphate buffer (pH 7.2) for 24 h. The samples were washed three times in 0.15 M sodium cacodylate buffer (pH 7.2) and then fixed again in 1% w/v OsO_4 in 0.12 M sodium cacodylate buffer (pH 7.2) for 2 h. The samples were dehydrated in a series of increasing ethanol concentrations, transferred to propylene oxide, and embedded in Epon. Eighty-nm-thick sections were cut with a Reichert-Jung Ultracut E microtome and collected on Formvar-coated copper grids. Staining of the sections was performed using uranyl acetate and lead citrate. The sections were imaged on a Phillips CM 100 BioTWIN

transmission electron microscope. Autophagosomes were quantified in 30–35 cells per sample as described previously [30].

Quantitative RT-PCR
RNA was isolated by using the NucleoSpin RNA Kit (Macherey-Nagel), according to the manufacturer's instructions. RT-PCR was performed by using the PowerUp SYBR Green Master Mix (Thermo Fisher Scientific). All primer sequences used are listed in Table S1.

Reverse transcriptase PCR
RNA was isolated with the NucleoSpin RNA Kit (Macherey-Nagel), according to the manufacturer's instructions. The reverse transcriptase was performed with the M-MLV reverse Transcriptase (Promega M1705) and the PCR was done with the GoTaq Hot Start Polymerase (Promega M5001) with the indicated GSK3B primers (Table S1). The samples were loaded on a 1% agarose gel, and the signal was visualized using an Amersham imager 600 (GE Healthcare).

Statistical methods
Statistical comparisons were carried out with the GraphPad Prism 8.0 software. All experiments were performed in biological triplicates and plotted as mean ± SD from three independent experiments, unless stated otherwise. Statistical significance was measured by an unpaired two-tailed t test. Significance in all figures is indicated as follows: ns (non-significant) $p > 0.05$, *$p < 0.05$, **$p < 0.01$, ***$p < 0.001$, ****$p < 0.0001$.

OPP protein synthesis assay
Global protein synthesis was assessed using the Click-iT™ Plus OPP Alexa Fluor™ 488 Protein Synthesis Assay Kit (C10428 ThermoFisher) according to the manufacturer's instructions. In brief, MCF-7 eGFP-LC3 cells were reverse transfected for 72 h and treated with 20 μM Click-it OPP for 30 min prior to fixation in 3.7% formaldehyde and permeabilization in 0,5% Triton X-100. The Click-it reaction was performed using Alexa Fluor 488, and nuclei were stained with Hoechst to register cell number in parallel. Image acquisition was done using an InCell2200 automated microscope equipped with a 20× Nikon objective (GE Healthcare). Six pictures were taken per well (counting >1500 cells per well) and fluorescent quantification and analysis was done using the InCell Analyzer Workstation 3.7.3 software (GE Healthcare). CHX treatment was for 5 min (100 μg/ml).

RNA sequencing
MCF-7 eGFP-LC3 cells were transfected for 72 h in triplicates for si ctrl, si eIF4A3 A, and si eIF4A3 B. RNA was isolated by using the NucleoSpin RNA Kit as described above. A total of nine samples were sequenced using the BGI DNBSeq platform. Low-quality, adapter-polluted, and high content of unknown base (N) reads were removed from the pool, and clean reads were mapped to GRCh38/hg38 reference genome using HISAT2 [49]. Differentially expressed genes were identified using DEseq2 [31] applying cut-offs of FC ≥2 and adjusted p value ≤0.05. Enrichment analysis was performed using the enrichR package [50] with GO_Biological_Process_2018 and GO_Cellular_Component_2018 as gene-set libraries. The script and data from the analyses are deposited at https://github.com/ELELAB/eIF4A3_RNASEQ.

Differential expression and correlation analysis of TCGA data
TCGA RNA-Seq data was downloaded, aggregated, and pre-processed using different functionalities of the TCGAbiolinks Bioconductor/R package version 2.12.5 [51]. We performed a differential gene expression analysis comparing tumor vs. normal samples using the limma-voom pipeline, based on an empirical Bayes procedure, as we implemented in TCGAbiolinks version 2 and higher [51]. We retained only those cancer types for which there were at least five normal tissue (NT) samples for comparison to tumor primary (TP) tissue samples, resulting in a total of 18 cancer types from which 14 (78%) displayed differentially expressed eIF4A3 (cut-off of FDR < 0.05). In all cases except for one (KICH), eIF4A3 was significantly upregulated. We performed a Spearman correlation analysis using the cor.test function in the R stats v. 3.6.2 package to investigate the correlation in mRNA expression between eIF4A3 and a compiled list of confirmed TFEB targets [8–10] (Table S2) in the seven cancer types displaying eIF4A3 upregulation of at least logFC > 0.5 (COAD, READ, GBM, ESCA, BRCA, LUSC, and LUAD). We performed a similar analysis for cancer subtypes, following the same selection criteria. The Spearman correlation

coefficient ranges between −1 and +1, where −1 is maximum negative correlation (blue) and +1 is maximum positive correlation (red). Genes with missing data points in more than half the samples were omitted to allow clustering. Clustering was performed on both columns and rows of the correlation matrices, using the clustering feature of the Complex-Heatmap package, and using Euclidean distance between elements and complete linkage hierarchical clustering. The script and data from the analyses are deposited at https://github.com/ELELAB/eIF4A3_RNASEQ.

Splicing analysis in rMATs
FASTQ raw sequence files were quality checked with FASTQC version 0.11.9 (http://www.bioinformatics.babraham.ac.uk/projects/fastqc). Low-quality reads and adapter sequences were trimmed with Trimmomatic version 0.36 [52]. Sequencing reads were further processed to a single length of 100 bp with Trimmomatic, to fulfill the length requirements of downstream splicing analysis with rMATS [32]. Starting from trimmed FASTQ sequence files, mapping and identification of transcriptome-wide splicing events was done simultaneously using rMATS turbo version 4.1.0 (http://rnaseq-mats.sourceforge.net/rmats4.1.0/). Mapping to the human genome assembly GRCh38.p13 (GENCODE release 33; https://www.gencodegenes.org/human/release_33.html) was performed by STAR aligner version 2.7.4 [53]. Identification of transcriptome-wide splicing events was performed using GENCODE GRCh38.p13 (release 33) GTF reference file as annotation. Samples after eIF4A3 knockdown (eIF4A3 targeting siRNA A or B transfected cells; each group with $n = 3$) were compared with the control group (si ctrl-transfected cells; $n = 3$) using a cut-off splicing difference of 0.05 (5%). Analysis of rMATS output splicing files was performed using maser package (https://github.com/DiogoVeiga/maser). Candidate alternative splicing events (SE, A5SS, A3SS, MXE, or RI) were defined considering reads that span junctions only (JC), as defined by rMATS. Further filtering was performed for those events with coverage >20, deltaPSI >0.1, and FDR < 0.01.

DATA AVAILABILITY
All datasets generated and analyzed in this study are deposited at the GitHub repository (https://github.com/ELELAB/eIF4A3_RNASEQ) or provided in the supplementary information files.

REFERENCES
1. Mizushima N. A brief history of autophagy from cell biology to physiology and disease. Nat Cell Biol. 2018;20:521–7.
2. Levine B, Kroemer G. Biological functions of autophagy genes: a disease perspective. Cell. 2019;176:11–42.
3. Poillet-Perez L, White E. Role of tumor and host autophagy in cancer metabolism. Genes Dev. 2019;33:610–9.
4. Vanzo R, Bartkova J, Merchut-Maya JM, Hall A, Bouchal J, Dyrskjot L, et al. Autophagy role(s) in response to oncogenes and DNA replication stress. Cell Death Differ. 2019;27:1134–53.
5. Di Malta C, Cinque L, Settembre C. Transcriptional regulation of autophagy: mechanisms and diseases. Front Cell Dev Biol. 2019;7:114.
6. Fullgrabe J, Ghislat G, Cho DH, Rubinsztein DC. Transcriptional regulation of mammalian autophagy at a glance. J Cell Sci. 2016;129:3059–66.
7. Steingrimsson E, Copeland NG, Jenkins NA. Melanocytes and the microphthalmia transcription factor network. Annu Rev Genet. 2004;38:365–411.
8. Sardiello M, Palmieri M, di Ronza A, Medina DL, Valenza M, Gennarino VA, et al. A gene network regulating lysosomal biogenesis and function. Science. 2009;325:473–7.
9. Settembre C, Di Malta C, Polito VA, Garcia Arencibia M, Vetrini F, Erdin S, et al. TFEB links autophagy to lysosomal biogenesis. Science. 2011;332:1429–33.
10. Palmieri M, Impey S, Kang H, di Ronza A, Pelz C, Sardiello M, et al. Characterization of the CLEAR network reveals an integrated control of cellular clearance pathways. Hum Mol Genet. 2011;20:3852–66.
11. Puertollano R, Ferguson SM, Brugarolas J, Ballabio A. The complex relationship between TFEB transcription factor phosphorylation and subcellular localization. EMBO J. 2018;37:e98804.
12. Li Y, Xu M, Ding X, Yan C, Song Z, Chen L, et al. Protein kinase C controls lysosome biogenesis independently of mTORC1. Nat Cell Biol. 2016;18:1065–77.
13. Roczniak-Ferguson A, Petit CS, Froehlich F, Qian S, Ky J, Angarola B, et al. The transcription factor TFEB links mTORC1 signaling to transcriptional control of lysosome homeostasis. Sci Signal. 2012;5:ra42.
14. Palmieri M, Pal R, Nelvagal HR, Lotfi P, Stinnett GR, Seymour ML, et al. mTORC1-independent TFEB activation via Akt inhibition promotes cellular clearance in neurodegenerative storage diseases. Nat Commun. 2017;8:14338.

15. Settembre C, Zoncu R, Medina DL, Vetrini F, Erdin S, Erdin S, et al. A lysosome-to-nucleus signalling mechanism senses and regulates the lysosome via mTOR and TFEB. EMBO J. 2012;31:1095–108.

16. Lubas M, Harder LM, Kumsta C, Tiessen I, Hansen M, Andersen JS, et al. eIF5A is required for autophagy by mediating ATG3 translation. EMBO Rep. 2018;19:e46072.

17. Linder P, Jankowsky E. From unwinding to clamping - the DEAD box RNA helicase family. Nat Rev Mol Cell Biol. 2011;12:505–16.

18. Chan CC, Dostie J, Diem MD, Feng W, Mann M, Rappsilber J, et al. eIF4A3 is a novel component of the exon junction complex. RNA. 2004;10:200–9.

19. Le Hir H, Gatfield D, Izaurralde E, Moore MJ. The exon-exon junction complex provides a binding platform for factors involved in mRNA export and nonsense-mediated mRNA decay. EMBO J. 2001;20:4987–97.

20. Wang Z, Murigneux V, Le Hir H. Transcriptome-wide modulation of splicing by the exon junction complex. Genome Biol. 2014;15:551.

21. Choe J, Ryu I, Park OH, Park J, Cho H, Yoo JS, et al. eIF4AIII enhances translation of nuclear cap-binding complex-bound mRNAs by promoting disruption of secondary structures in 5'UTR. Proc Natl Acad Sci USA. 2014;111:E4577–4586.

22. Nott A, Le Hir H, Moore MJ. Splicing enhances translation in mammalian cells: an additional function of the exon junction complex. Genes Dev. 2004;18:210–22.

23. Blazquez L, Emmett W, Faraway R, Pineda JMB, Bajew S, Gohr A, et al. Exon junction complex shapes the transcriptome by repressing recursive splicing. Mol Cell. 2018;72:496.e9–509.e9.

24. Boehm V, Britto-Borges T, Steckelberg AL, Singh KK, Gerbracht JV, Gueney E, et al. Exon junction complexes suppress spurious splice sites to safeguard transcriptome integrity. Mol Cell. 2018;72:482.e7–95.e7.

25. Michelle L, Cloutier A, Toutant J, Shkreta L, Thibault P, Durand M, et al. Proteins associated with the exon junction complex also control the alternative splicing of apoptotic regulators. Mol Cell Biol. 2012;32:954–67.

26. Mazloomian A, Araki S, Ohori M, El-Naggar AM, Yap D, Bashashati A, et al. Pharmacological systems analysis defines EIF4A3 functions in cell-cycle and RNA stress granule formation. Commun Biol. 2019;2:165.

27. Ryu I, Won YS, Ha H, Kim E, Park Y, Kim MK, et al. eIF4A3 phosphorylation by CDKs affects NMD during the cell cycle. Cell Rep. 2019;26:2126.e9–39.e9.

28. Klionsky DJ, Abdelmohsen K, Abe A, Abedin MJ, Abeliovich H, Acevedo Arozena A, et al. Guidelines for the use and interpretation of assays for monitoring autophagy (3rd edition). Autophagy. 2016;12:1–222.

29. Holdgaard SG, Cianfanelli V, Pupo E, Lambrughi M, Lubas M, Nielsen JC, et al. Selective autophagy maintains centrosome integrity and accurate mitosis by turnover of centriolar satellites. Nat Commun. 2019;10:4176.

30. Tiessen I, Abildgaard MH, Lubas M, Gylling HM, Steinhauer C, Pietras EJ, et al. A high-throughput screen identifies the long non-coding RNA DRAIC as a regulator of autophagy. Oncogene. 2019;38:5127–41.

31. Love MI, Huber W, Anders S. Moderated estimation of fold change and dispersion for RNA-seq data with DESeq2. Genome Biol. 2014;15:550.

32. Shen S, Park JW, Lu ZX, Lin L, Henry MD, Wu YN, et al. rMATS: robust and flexible detection of differential alternative splicing from replicate RNA-Seq data. Proc Natl Acad Sci USA. 2014;111:E5593–5601.

33. Manning G, Whyte DB, Martinez R, Hunter T, Sudarsanam S. The protein kinase complement of the human genome. Science. 2002;298:1912–34.

34. Abildgaard MH, Brynjolfsdottir SH, Frankel LB. The Autophagy-RNA Interplay: Degradation and Beyond. Trends Biochem Sci. 2020;45:845–57.

35. Gatica D, Hu G, Liu X, Zhang N, Williamson PR, Klionsky DJ. The Pat1-Lsm complex stabilizes ATG mRNA during nitrogen starvation-induced autophagy. Mol Cell. 2019;73:314.e4–24.4.

36. Tang HW, Hu Y, Chen CL, Xia B, Zirin J, Yuan M, et al. The TORC1-regulated CPA complex rewires an RNA processing network to drive autophagy and metabolic reprogramming. Cell Metab. 2018;27:1040.e8–54.e8.

37. Xu G, Li T, Chen J, Li C, Zhao H, Yao C, et al. Autosomal dominant retinitis pigmentosa-associated gene PRPF8 is essential for hypoxia-induced mitophagy through regulating ULK1 mRNA splicing. Autophagy. 2018;14:1818–30.

38. Zhang H, Alsaleh G, Feltham J, Sun Y, Napolitano G, Riffelmacher T, et al. Polyamines control eIF5A hypusination, TFEB translation, and autophagy to reverse B cell senescence. Mol Cell. 2019;76:110.e9–25.e9.

39. Medina DL, Di Paola S, Peluso I, Armani A, De Stefani D, Venditti R, et al. Lysosomal calcium signalling regulates autophagy through calcineurin and TFEB. Nat Cell Biol. 2015;17:288–99.

40. Ito M, Iwatani M, Kamada Y, Sogabe S, Nakao S, Tanaka T, et al. Discovery of selective ATP-competitive eIF4A3 inhibitors. Bioorg Med Chem. 2017;25:2200–9.

41. Iwatani-Yoshihara M, Ito M, Ishibashi Y, Oki H, Tanaka T, Morishita D, et al. Discovery and characterization of a eukaryotic initiation factor 4A-3-selective inhibitor that suppresses nonsense-mediated mRNA decay. ACS Chem Biol. 2017;12:1760–8.

42. Mizojiri R, Nakata D, Satoh Y, Morishita D, Shibata S, Iwatani-Yoshihara M, et al. Discovery of novel 5-(piperazine-1-carbonyl)pyridin-2(1H)-one derivatives as orally eIF4A3-selective inhibitors. ACS Med Chem Lett. 2017;8:1077–82.

43. Ito M, Tanaka T, Cary DR, Iwatani-Yoshihara M, Kamada Y, Kawamoto T, et al. Discovery of novel 1,4-diacylpiperazines as selective and cell-active eIF4A3 inhibitors. J Med Chem. 2017;60:3335–51.

44. Nezich CL, Wang C, Fogel AI, Youle RJ. MiT/TFE transcription factors are activated during mitophagy downstream of Parkin and Atg5. J Cell Biol. 2015;210:435–50.

45. Settembre C, De Cegli R, Mansueto G, Saha PK, Vetrini F, Visvikis O, et al. TFEB controls cellular lipid metabolism through a starvation-induced autoregulatory loop. Nat Cell Biol. 2013;15:647–58.

46. Decressac M, Mattsson B, Weikop P, Lundblad M, Jakobsson J, Bjorklund A. TFEB-mediated autophagy rescues midbrain dopamine neurons from alpha-synuclein toxicity. Proc Natl Acad Sci USA. 2013;110:E1817–26.

47. Tsunemi T, Ashe TD, Morrison BE, Soriano KR, Au J, Roque RA, et al. PGC-1alpha rescues Huntington's disease proteotoxicity by preventing oxidative stress and promoting TFEB function. Sci Transl Med. 2012;4:142ra197.

48. Spampanato C, Feeney E, Li L, Cardone M, Lim JA, Annunziata F, et al. Transcription factor EB (TFEB) is a new therapeutic target for Pompe disease. EMBO Mol Med. 2013;5:691–706.

49. Kim D, Langmead B, Salzberg SL. HISAT: a fast spliced aligner with low memory requirements. Nat Methods. 2015;12:357–60.

50. Kuleshov MV, Jones MR, Rouillard AD, Fernandez NF, Duan Q, Wang Z, et al. Enrichr: a comprehensive gene set enrichment analysis web server 2016 update. Nucleic Acids Res. 2016;44:W90–97. W1

51. Mounir M, Lucchetta M, Silva TC, Olsen C, Bontempi G, Chen X, et al. New functionalities in the TCGAbiolinks package for the study and integration of cancer data from GDC and GTEx. PLoS Comput Biol. 2019;15:e1006701.

52. Bolger AM, Lohse M, Usadel B. Trimmomatic: a flexible trimmer for Illumina sequence data. Bioinformatics. 2014;30:2114–20.

53. Dobin A, Davis CA, Schlesinger F, Drenkow J, Zaleski C, Jha S, et al. STAR: ultrafast universal RNA-seq aligner. Bioinformatics. 2013;29:15–21.

AUTHOR CONTRIBUTIONS
LBF developed the study concept; DS, THK, MHA, ARL, and LBF performed experiments; LB, MT, EP, and THK analyzed the sequencing and TCGA data; LBF, EP, and JB provided supervision; LBF, DS, and THK wrote the manuscript; all authors read and approved the final manuscript.

ETHICAL APPROVAL
The study did not require any ethical approval.

COMPETING INTERESTS
The authors declare no competing interests.

ADDITIONAL INFORMATION
Supplementary information The online version contains supplementary material available at https://doi.org/10.1038/s41418-021-00822-y.

Correspondence and requests for materials should be addressed to L.B.F.

Reprints and permission information is available at http://www.nature.com/reprints

Publisher's note Springer Nature remains neutral with regard to jurisdictional claims in published maps and institutional affiliations.